Tribology International 90 (2015) 343–355

Contents lists available at ScienceDirect

Tribology International

journal homepage: www.elsevier.com/locate/triboint

A numerical framework for discrete modelling of friction and wear using Voronoi polyhedrons

Guilhem Mollon *

Université de Lyon, INSA Lyon, LaMCoS, UMR CNRS 5259, France

ARTICLE INFO

Article history:
Received 22 December 2014
Received in revised form
2 April 2015
Accepted 7 April 2015
Available online 23 April 2015

Keywords:
Dry friction
Wear
Discrete modelling
Voronoi polyhedrons

ABSTRACT

In this work, we present a numerical framework for the modelling of friction and wear of rough surfaces. This framework is based on the Discrete Element Method (DEM), and aims to mimic the inner microstructure of polycrystalline materials. For this purpose, a sample generation program has been developed, into which each grain of this microstructure is represented by a rigid 3D Voronoi cell. A typical sample generated by this program represents a body composed of a degradable and a non-degradable parts, both of which presenting several well-controlled features: size and geometry of the grains (controlled by the positions of the seeding points of the Voronoi tessellation), roughness of the surface and of the underlying substrate (controlled by the means of the frequency content and possible anisotropy of this roughness), and periodic or planar lateral boundaries. These features enable the modelling of a large number of contact situations with a great flexibility. After presenting in details the algorithmic routines developed for this sample generation, we detail some examples of generated samples and we provide insight of their implementation in the implicit discrete code LMGC90. An Illustrative simulation is then performed to demonstrate the ability of this framework to model diverse situations of friction and wear, by representing accurately the creation and the rheology of third bodies.

1. Introduction

The understanding and prediction of friction and wear occupy a central position in tribology, and these phenomena may be efficiently described in the context of the tribological triplet which was first proposed by Godet and Berthier [1,2]. In this conceptual framework, a frictional contact is investigated at three different scales which form the tribological triplet: the scale of the mechanism surrounding the contact, the scale of the two bodies in contact (called first-bodies), and the scale of the so-called third-body, i.e. the interfacial material coming from the degradation of first-bodies or entering into the contact from the outside. This last scale is particularly complicated to study, because it is the place for many mechanical transformations (damage, fracture, fatigue, plasticity, phase change, etc.), many physical phenomena (heat production, chemical reactions, electrostatic interactions, etc.) and because its confinement prevents it from a convenient experimental measurement. Observations of third-body in various contact conditions [3,4] reveal that it may be more or less heterogeneous and continuous, that its thickness may have various orders of magnitudes (from a few nanometres to several micrometres), that a large part of its content comes from the degradation of first-bodies, and that it flows into the contact with an unknown rheology. Continuous modelling [5,6] of such a medium is very challenging, because it involves very large deformations, frequent discontinuities, and complex constitutive laws. Alternatively, successful attempts have been made by the numerical tribology community to apply the concepts of Discrete Element Modelling (DEM) to this specific problem. These techniques are now rather common in the field of granular materials [7–9], and offer the kinematic flexibility that lacks in continuum approaches since they consist in representing the motion of each body composing a granular assembly, and thus do not rely on any continuity assumption. Recent works on granular matter have consisted in introducing more and more complex [10–14] and realistic [15–18] granular shapes in such simulations, inspired by the progress of the experimental assessment of granular morphologies [19,20]. In the field of tribology, however, realistic shapes have not been very much investigated since the DEM is more used as a convenient tool to represent the flow of matter in a phenomenological way [21–23] than as a close reproduction of the micromechanical behaviour of the third-bodies. Rather, efforts have been put in using more sophisticated or realistic contact laws in order for the numerical phenomenology to approach the experimental one [24–26]. In the last decade, DEM has been often used in tribology to model the first body degradation and the third-body flow [27–29], and current trends consist in coupling discrete

* Tel.: +33 472438937; fax: +33 478890980.
E-mail address: guilhem.mollon@gmail.com

http://dx.doi.org/10.1016/j.triboint.2015.04.011
0301-679X/

methods with finite elements to perform multi-scale modelling [30], or in enriching the models with other physical ingredients such as heat or electricity [31–33].

Interestingly, the DEM has also been used in the field of fracture mechanics, to model the initiation and propagation of cracks in materials [34–37]. In particular, the work of Sadeghi and co-workers on rolling contact fatigue [38–40] is of great interest, because it deals with microstructural cracks which develop at the scale of interest for tribologists. In these papers, the microstructure of a polycrystalline material is represented at small scale by a Voronoi tessellation, and each cell of this tessellation is then considered as an independent rigid body subjected to the laws of motions. This approach is then used in a DEM framework to study the microstructural damage of the material. In the present paper, we wish to use concepts developed in this set of papers to propose a DEM framework for the modelling of the superficial degradation of first-bodies subjected to frictional contact, and then to follow the evolution of the damaged material as a third-body within the tribological interface. The present work mostly focuses on methodological statements about the generation and implementation of such a model, and proposes several evolutions which might be implemented in further studies to improve our understanding and prediction of friction and wear.

2. Sample generation

2.1. Principle of the method

In this paper, the surface of a solid object is modelled in a simplified way, using the schematization presented in Fig. 1. We focus on a portion of this surface represented by a rectangular domain of dimensions L_x and L_y. The z-axis corresponds to the direction normal to the solid surface (this direction will be considered as vertical in this work). Since we are interested in the modelling of phenomena such as friction and wear, it is interesting to consider a certain degradable depth H of the material composing the solid surface. Hence, the model accounts for a certain volume of material, delimited by two surfaces S_x and S_x' along the x-axis, two surfaces S_y and S_y' along the y-axis, and two surfaces S_z and S_z' along the z-axis. The four lateral surfaces may be planar (i.e. the sample may be delimited by vertical walls), but they may also represent periodic geometric boundaries. In the most common case, the surface S_z might exhibit some roughness, as well as the lower horizontal boundary S_z'. In some situations, the average depth H of S_z' may represent a distance from the surface at which such phenomena as wear and degradation have a limited effect, and its choice will thus strongly depend on the considered material and on the contact conditions. In other situations, it may also represent the depth of a soft coating on a harder material, or a change of the mechanical properties of the material composing the solid. In any case, however, we suppose that the volume of interest (called "superficial layer" or "degradable first body" in this work, and represented in pink in Fig. 1) lies on an underlying material (called "substrate" or "non-degradable first body", in light blue in Fig. 1), which is considered as perfectly rigid and will be used as a lower boundary condition. The lower border of this substrate is a surface S_z'' with an arbitrary geometry.

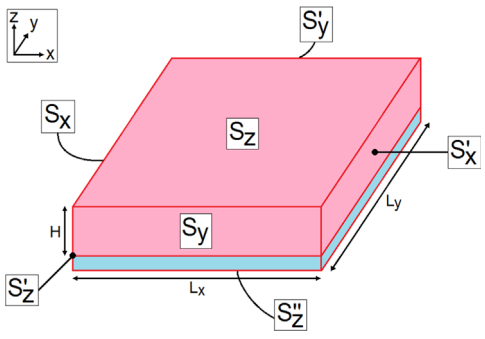

Fig. 1. Layout of the generated samples. (For interpretation of the references to color in this figure legend, the reader is referred to the web version of this article.)

In order to represent the evolution of the superficial layer submitted to a frictional contact and the possible creation of third body, it is desirable to introduce its microstructure in a geometrically relevant way. In this work, this microstructure is modelled by the means of a large number of polyhedral objects which form a complete partition of the superficial layer. The underlying assumption is that most of the deformation and degradation of the material will be related to relative motions located at the joints between these polyhedrons, which will thus be considered as individually rigid. Hence, the scope of this work is restricted to materials exhibiting a discrete microstructure, such as polycrystalline materials for example, and the case of amorphous materials may not be properly accounted for in the present model.

In order to generate these polyhedrons (which will be termed as "grains" in the remainder of this paper), a Voronoi tessellation is adopted. This common approach is implemented in many commercial computational packages, and provides a partition of an infinite space of arbitrary dimension, based on a given set of seeding points. Each "Voronoi cell" is attached to a certain seeding point P, and describes a portion of the space corresponding to the set of all the points which are closer to P than to any other seeding point. The Voronoi cells are convex, they do not overlap, and their union covers the totality of the considered space. In 3D, at the heart of the cloud of seeding point, they are convex polyhedrons and can readily represent the microstructure of a material. However, when approaching the border of the cloud of seeding points, most of these cells are "open" because they have some infinite dimensions. Hence, the method of sample generation proposed in this paper will consist in creating a set of seeding points in the superficial layer and in the substrate, perform a Voronoi tessellation to generate the corresponding cells, and apply some special techniques to deal with the cells located at the boundaries. The remainder of this section will detail the algorithms developed in order to generate the rough geometries of the surfaces S_z and S_z', to generate a proper microstructure in the neighbourhood of these surfaces, and finally to deal with the lateral geometric conditions.

2.2. Generation of rough surfaces

For numerical purposes, the surfaces S_z and S_z' are defined in a discrete way, using a fixed mesh on the rectangular domain. More specifically, the domain of dimensions $L_x \times L_y$ is discretized into $N_x \times N_y$ identical rectangular elements, each of which is then divided into two triangles. Assigning a given elevation $z(n_x, n_y)$ to each node of this grid thus defines an univocal triangulated surface, which represents an acceptable approximation of a real surface if the mesh is fine enough. In any case, each triangular facets should be small enough when compared to the typical scale of fluctuation of the surface elevation, and the appropriate mesh fineness is thus strongly problem-dependant. In the present case, the values $N_x = N_y = 100$ are used.

There is a rich scientific literature about the characterization of morphologies of real surfaces at diverse scales (e.g. [41,42]). Without loss of generality, we employ in the present work a simple method of surface generation based on discrete random fields. Such fields are widely used in many scientific and engineering areas [43–45,17], and several mathematical methods of generation have been proposed in order, for example, to deal with non-Gaussian probability density functions or with complicated autocorrelation patterns [46,47]. For the sake of simplicity, the one we use in this work is very basic and is based on the discrete 2D Fourier transform. The frequency content of

the surface roughness is controlled by the means of a user-defined 2D discrete spectrum, defined on the abstract space of the 2D Fourier modes. More specifically, one has to choose the (real) amplitudes $A(n_x, n_y)$ of the Fourier modes (n_x, n_y), with the following constraints:

$$1 \le n_x \le N_x+1 \quad \text{and} \quad 1 \le n_y \le N_y+1 \tag{1}$$

$$A(n_x, N_y/2+1) = 0 \quad \forall n_x \quad \text{and} \quad A(N_x/2+1, n_y) = 0 \quad \forall n_y \tag{2}$$

$$A(n_x, n_y) = A(n_x, N_y+2-n_y) \quad \forall n_x \tag{3}$$

$$A(n_x, n_y) = A(N_x+2-n_x, n_y) \quad \forall n_y \tag{4}$$

In other words, the amplitude of the 2D spectrum should be defined on the $(N_x+1) \times (N_y+1)$ discrete space, be null on the row $N_y/2+1$ and on the column $N_x/2+1$, and symmetric with respect to this row and this column. Again, for the sake of simplicity and without any loss of generality, we adopt here the following general formulation for the input spectrum:

$$A(n_x, n_y) = \exp\left[-\lambda_x(n_x - n_{x0}) - \lambda_y(n_y - n_{y0})\right]$$
$$\text{for} \quad n_{x0} \le n_x \le N_x/2 \quad \text{and} \quad n_{y0} \le n_y \le N_y/2$$
$$A(n_x, n_y) = 0 \quad \text{elsewhere} \tag{5}$$

hence, we set the amplitude of a fundamental mode (n_{x0}, n_{y0}) to 1, and we apply an exponential decay of parameters λ_x in the x-direction and λ_y in the y-direction, before applying the symmetry conditions (3) and (4). Each of these modes is then attributed a phase angle $\theta(n_x, n_y)$, randomly sampled between $-\pi$ and π. Once again, a specific symmetry condition is to be applied:

$$\theta(n_x, n_y) = -\theta(N_x+2-n_x, N_y+2-n_y) \tag{6}$$

Then, the complex Fourier spectrum is computed by

$$Z(n_x, n_y) = A(n_x, n_y)\exp\left[i \cdot \theta(n_x, n_y)\right] \tag{7}$$

A random discrete 2D signal $z_c(n_x, n_y)$ is then obtained directly by a 2D Fast Fourier Transform (FFT) applied to $Z(n_x, n_y)$. If conditions (1)–(4) and (6) are verified, this signal is real. Finally, the current standard deviation σ_c of the field is computed, and the final surface $z(n_x, n_y)$ is obtained after scaling, in order to match a desired mean value μ and a desired standard deviation σ:

$$z(n_x, n_y) = z_c(n_x, n_y)\frac{\sigma}{\sigma_c} + \mu \tag{8}$$

Three examples are provided in Fig. 2. For each one, the left-hand column describes the discrete amplitude decay in the x and y directions, the central column provides the amplitude of the whole

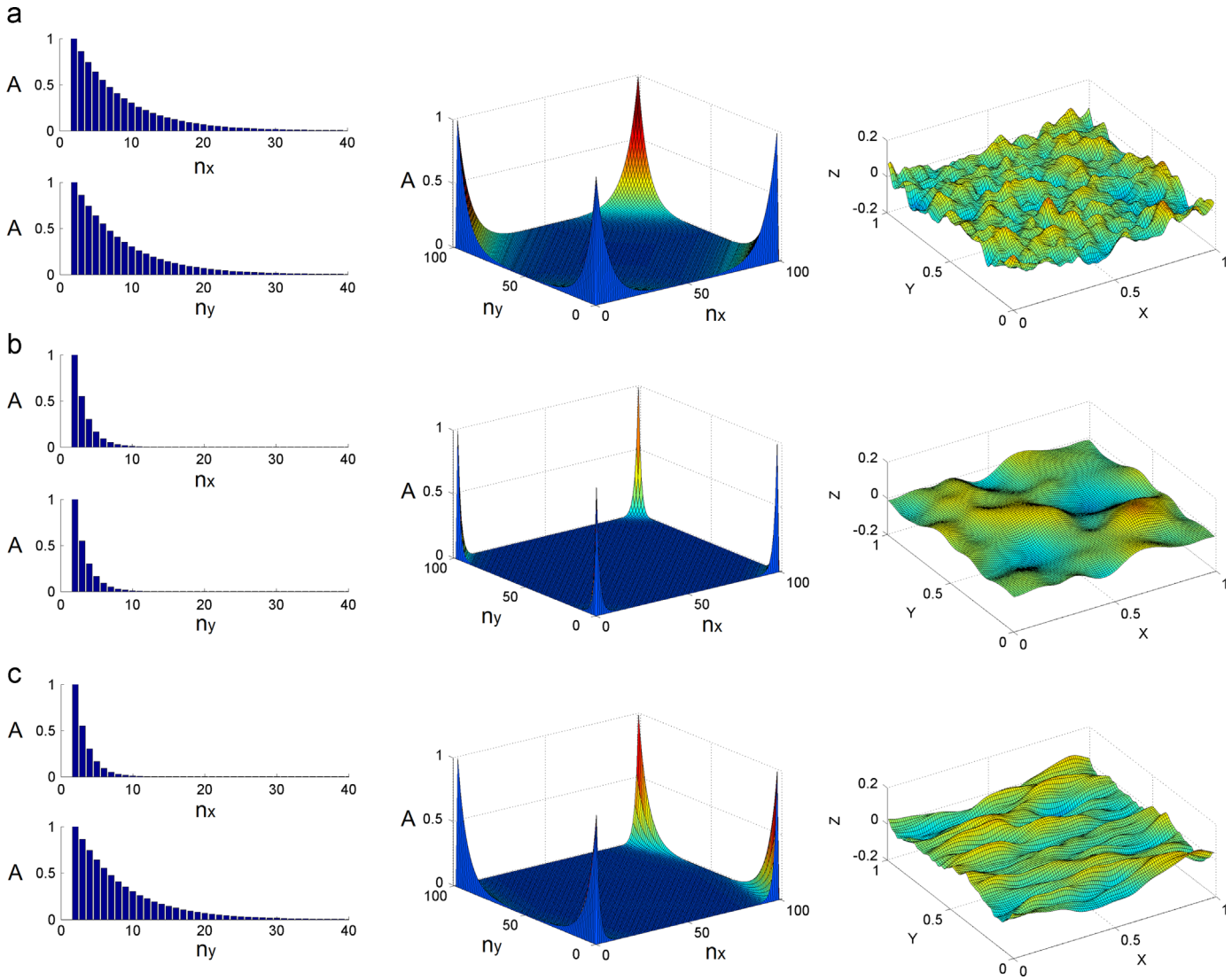

Fig. 2. Examples of rough surface generation on the unit square, with $N_x = N_y = 100$, $n_{x0} = n_{y0} = 2$, $\mu = 0$, and $\sigma = 0.03$; (a) $\lambda_x = \lambda_y = 0.15$; (b) $\lambda_x = \lambda_y = 0.6$; (c) $\lambda_x = 0.6$ and $\lambda_y = 0.15$

2D spectrum, and the right-hand column provides an illustrative realization of the rough surface on the unit square, for a given set of random phase angles. From this figure, we observe that the generated surfaces are bi-periodic, and that a good control is achieved on the amplitudes and frequencies of the roughness in both x and y directions. This methodology will be used in the remainder of this paper, but any other method of surface generation may be applied as well in the framework described hereafter.

2.3. Discretization of the upper face

As stated in a previous subsection, the use of Voronoi tessellation provides a nice set of conforming and non-overlapping convex polyhedrons at the heart of the cloud of seeding points, but leads to open cells when close to a border of this cloud. Hence, if one wants to partition the volume of degradable first body presented in Fig. 1 with convex polyhedrons, special treatments have to be applied in the neighbourhood of the upper, lower, and lateral faces. These techniques are presented in this subsection and the next two ones. To illustrate the techniques described in these subsections, Figs. 3–5 provide illustrations of the employed algorithms in a 2D case. This simplification is used here to ease understanding, but the actual methods that were developed are in 3D and rely on the same concepts.

Fig. 3a presents a random cloud of seeding points. A typical distance d between neighbouring points is computed in the following way:

$$d = \sqrt{S_{tot}/n} \quad \text{in } 2D \tag{9}$$

$$d = \sqrt[3]{V_{tot}/n} \quad \text{in } 3D \tag{10}$$

In these expressions, S_{tot} (respectively V_{tot}) represents the total surface (respectively volume) into which n seeding points have been generated. Fig. 3b presents a random curve crossing this cloud and representing in 2D the desired upper surface S_z. This surface is discrete, i.e. it is a set of segments in the 2D case, and a set of triangular facets in the 3D case, as explained in Section 2.2. From Fig. 3c, it clearly appears that a direct application of a Voronoi tessellation of the cloud of points will not lead to acceptable results. A simple technique would consist in computing the intersections of the curve with the cells it crosses, and to keep only the portions of cells located below the curve. This approach, however, often leads to complicated intersection patterns with very small and very elongated cells (e.g. in black circles in Fig. 3c), which may lead to a superficial microstructure different from the one in the bulk of the material. To overcome this drawback, it is necessary to ensure that S_z only crosses large cells close to their middle, in order for the lower parts of these cut cells to be large enough. To perform this, we first delete all the seeding points closer to S_z than a certain distance $d_1 = (\alpha_1^2 d)$ (Fig. 3d). A typical value of $\alpha_1 = 1$ seems to provide acceptable results. In 3D, the closest distance from a seeding point P to the surface S_z is not difficult to compute since this surface is triangulated. Hence, a closest projection of a given point P on S_z only requires a very fast discrete search. This projected point may be a node of the triangulated surface or lie on an edge or on a facet, and directly provides the distance from the seeding point P to S_z.

After this stage, additional seeding points are input at random positions on S_z (blue dots in Fig. 3e), and a Voronoi tessellation is finally performed (Fig. 3f). In this tessellation, S_z only crosses large cells in their middle, and it is easy to determine their intersections with the rough curve/surface (green squares in Fig. 3g). In 2D, these intersection points are then linked by segments in order to close the lower parts of the cut cells, the upper parts are deleted as well as all the cells located above the curve, and these operations result in a satisfactory approximation of S_z with a proper underlying microstructure (Fig. 3h). In 3D, the intersections of the cells edges with S_z are also easy to compute since this surface is piecewise bilinear. Closing the lower part of a given cut cell, however, is not straightforward since the different intersections of the cell's edges with S_z are generally not coplanar. Hence, the vertices of the cell located below S_z and its intersection points with S_z are altogether submitted to a convex-hull algorithm, which results in a new convex cell with all the vertices located below or exactly on S_z.

2.4. Discretization of the lower face

This last observation (the non-coplanarity of the points of intersection of a polyhedral cell with a non-planar surface) is the reason why the method used to discretize the lower face S_z' is slightly different from the one presented for S_z in the previous subsection. Indeed, it is impossible to use a non-planar surface to divide a given cell into two conforming convex polyhedrons (at least one of them will have to be non-convex). This is not an issue in the case of S_z because the upper part is discarded, but it prevents from using the same method to define the surface S_z' separating the superficial layer and the substrate. An alternative method, illustrated in Fig. 4, is proposed. Fig. 4a–c presents the same kind of situation than in the previous subsection, with the same difficulties in Fig. 4c if a Voronoi tessellation is performed directly in the initial cloud of seeding points. Instead of this, we propose to delete all the seeding points that are either (i) located below S_z' and within a distance $d_2 = (\alpha_2^2 d)$ or (ii) located above S_z' and within a distance $d_3 = (\alpha_3^2 d)$ (Fig. 4d). The values $\alpha_2 = 4$ and $\alpha_3 = 0.1$ seem to provide satisfactory results. Then, the remaining points located above S_z' and within a distance d_2 (Blue dots in Fig. 4d) are "mirrored", i.e. copied in the lower part of the surface at a symmetrical position with respect to their closest projection on S_z' (Fig. 4e). A Voronoi tessellation is then performed and results in a set of cells, with the desired surface being approximated by the joints between some of them (Fig. 4f). This approximation is better when the cloud of seeding points is dense and when the curvature of the target surface is limited, but will always result in a more approximate surface than with the procedure described in Section 2.3. However, it provides a separation of the considered space into two sets of conforming convex polyhedrons. Depending on the problem to be treated, the surface S_z' may be taken as the one defined in the previous stages (the interface between the superficial layer and the substrate will then respect the input roughness, Fig. 4g), or as the one located above the first layer of cells (the interface will then present the same level of entanglement than in the microstructure of the bulk material (Fig. 4h).

2.5. Discretization of the lateral faces

At the lateral faces S_x, S_x', S_y and S_y', two different kinds of geometrical conditions may be introduced. These faces may be perfectly planar walls (which makes it possible to apply well-controlled force or displacement boundary conditions on them), or may present a geometrical periodicity (which makes it possible to model an infinite surface with a controlled periodicity). This second case relies on the fact that the rough surfaces S_z and S_z' were made bi-periodic in the method described in Section 2.2. Moreover, these geometric boundary conditions are not coupled, which means that one may apply one type of condition in the x-direction and the other one in the y-direction. Fig. 5a presents such a situation, with a cloud of seeding points defined in a 2D $L_x \times L_y$ rectangular domain. Fig. 5b shows the Voronoi tessellation applied directly on this cloud of points, and illustrates the difficulties related to open cells at the domain boundaries. In Fig. 5c, a method is proposed to enforce a wall-type geometric condition in the x-direction. This method is similar to that used in the previous subsection, and was also used in [15, 17] for bounded Voronoi tessellation of a convex domain. Each seeding point closer to the plane S_x than a given distance $d_4 = (\alpha_4^2 d)$

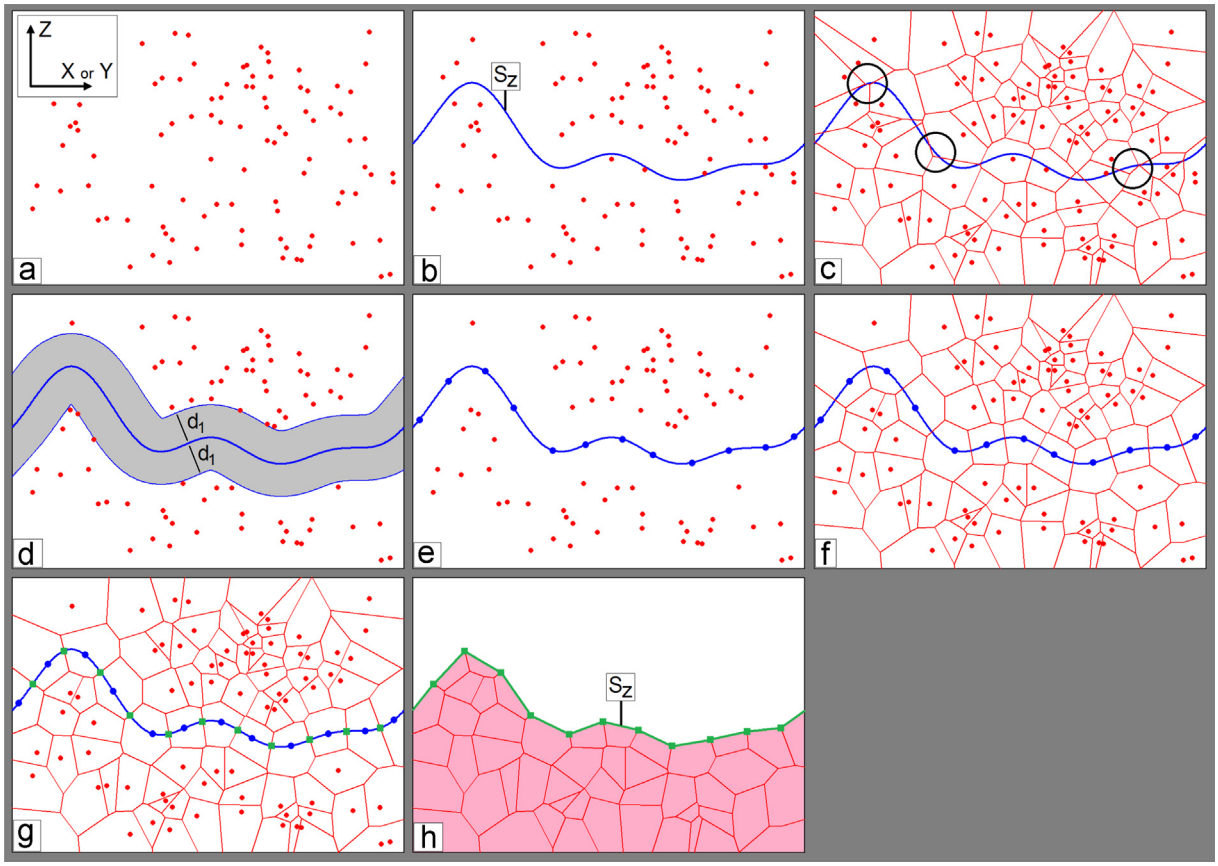

Fig. 3. 2D illustration of the technique used to discretize the rough upper surface. (For interpretation of the references to color in this figure legend, the reader is referred to the web version of this article.)

is mirrored (i.e. copied at a symmetric position with respect to its orthogonal projection on S_x), and the same operation is performed for S_x'. On the other hand, Fig. 5d shows how to enforce a periodic geometric condition in the y-direction. Each seeding point closer to the plane S_y than the distance d_4 is copied at a new position, with the same x-coordinate and a y-coordinate shifted by a distance L_y equal to the desired periodicity. The same operation is performed for S_y', with a y-shift equal to $-L_y$. As shown in Fig. 5d, these operations need also to be performed on the seeding points added when previously dealing with the surfaces S_x and S_x'. A typical value of $a_4 = 5$ is found to provide good results. A Voronoi tessellation is then performed (Fig. 5e), and only the Voronoi cells corresponding to the initial cloud of seeding points are kept (Fig. 5f). These cells present the desired geometric properties, i.e. in the present case they form planar walls in the x-direction and a geometric periodicity in the y-direction. The techniques presented in this subsection and in the two previous ones are implemented in the software MATLAB, and are applied on a 3D illustrative sample in Fig. 6, with various lateral geometric conditions.

3. Examples

3.1. Dimensions of sample and number of cells

Fig. 7 presents four illustrative samples generated on the unit square domain with bi-periodic boundaries. The same parameters are used for the random generations of the upper surfaces (i.e. $n_{x0} = n_{y0} = 2$, $\sigma = 0.02$, and $\lambda_x = \lambda_y = 0.6$). The samples shown in Fig. 7a and b illustrate the effect of the number of seeding points introduced in the volume of the superficial layer with the same average depth $H = 0.2$, since they respectively contain 1000 cells and 20,000 cells. It clearly appears that the number of cells should not be too small if one wants to render properly the desired statistical properties of the upper surface, especially when this surface has important local curvatures. Fig. 7c and d possess respectively 2500 and 7500 cells for respective average depths $H = 0.1$ and $H = 0.3$, and illustrate how the method of sample generation allows for various dimensions of the volume of degradable first body with similar grain size.

3.2. Microstructure of the material

In Fig. 8, several examples of possible microstructures are presented, all of which containing 5000 cells on a unit square domain with an average depth $H = 0.2$, and the same roughness parameters. Wall-type lateral conditions are applied to represent the intersections of these microstructures with vertical planes. Fig. 8a and b illustrates the cases of regular microstructures, for which the seeding points are located on regular lattices (a cubic and a hexagonal lattice respectively). The case presented in Fig. 8c is analogous to that of Fig. 8b (i.e. regular hexagonal lattice), except that a small perturbation is applied to render it more realistic. Each seeding point is positioned on the lattice, and then moved from a small distance in a random direction of space. This distance is randomly chosen in the interval $[0, d_r]$, where $d_r = (a_r^2 d)$ is a fraction of the average distance between two seeding points as described in Eq. (10). In the case of Fig. 8c we took $a_r = 0.2$, but this parameter may be different and bring an additional degree of freedom in the definition of the material microstructure. Choosing large values of a_r (typically larger than 1) leads to a distribution similar to that of a perfectly random cloud of points.

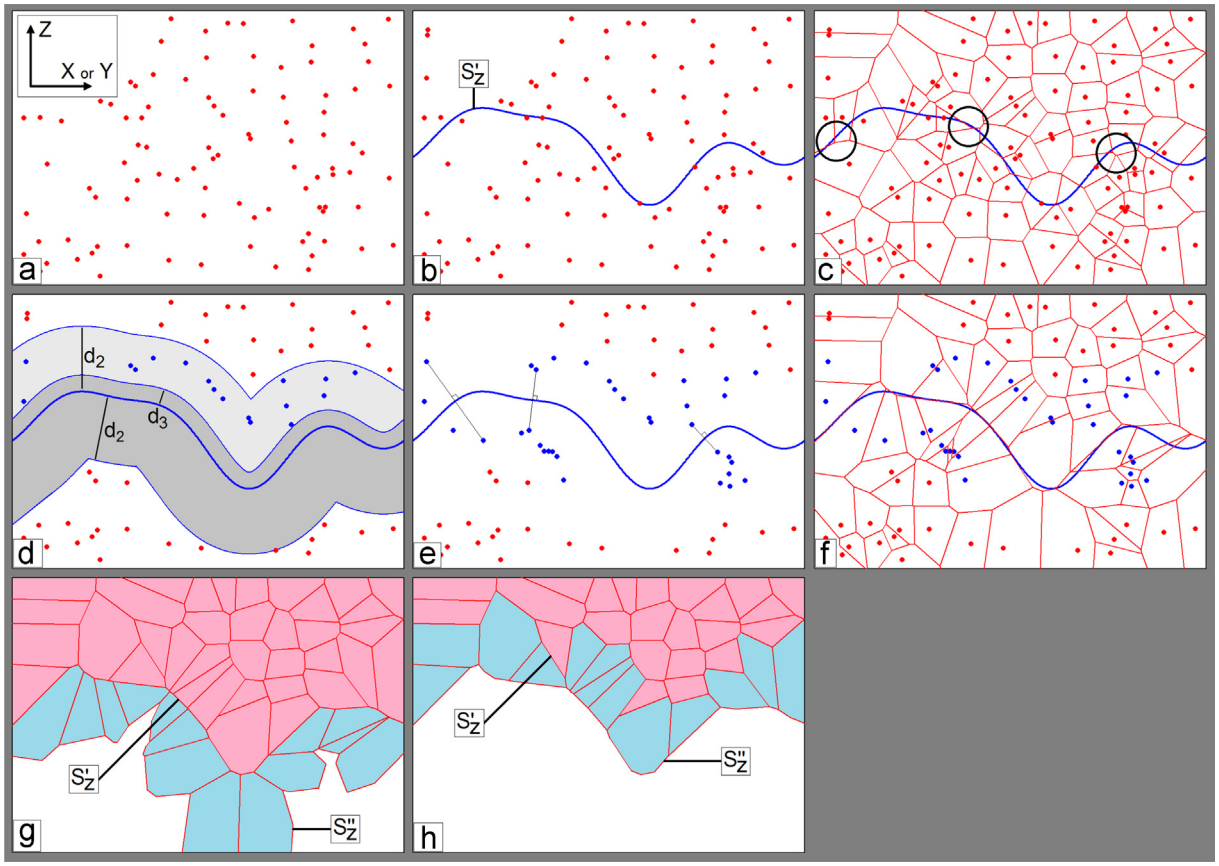

Fig. 4. 2D illustration of the technique used to discretize the rough lower surface and the substrate. (For interpretation of the references to color in this figure legend, the reader is referred to the web version of this article.)

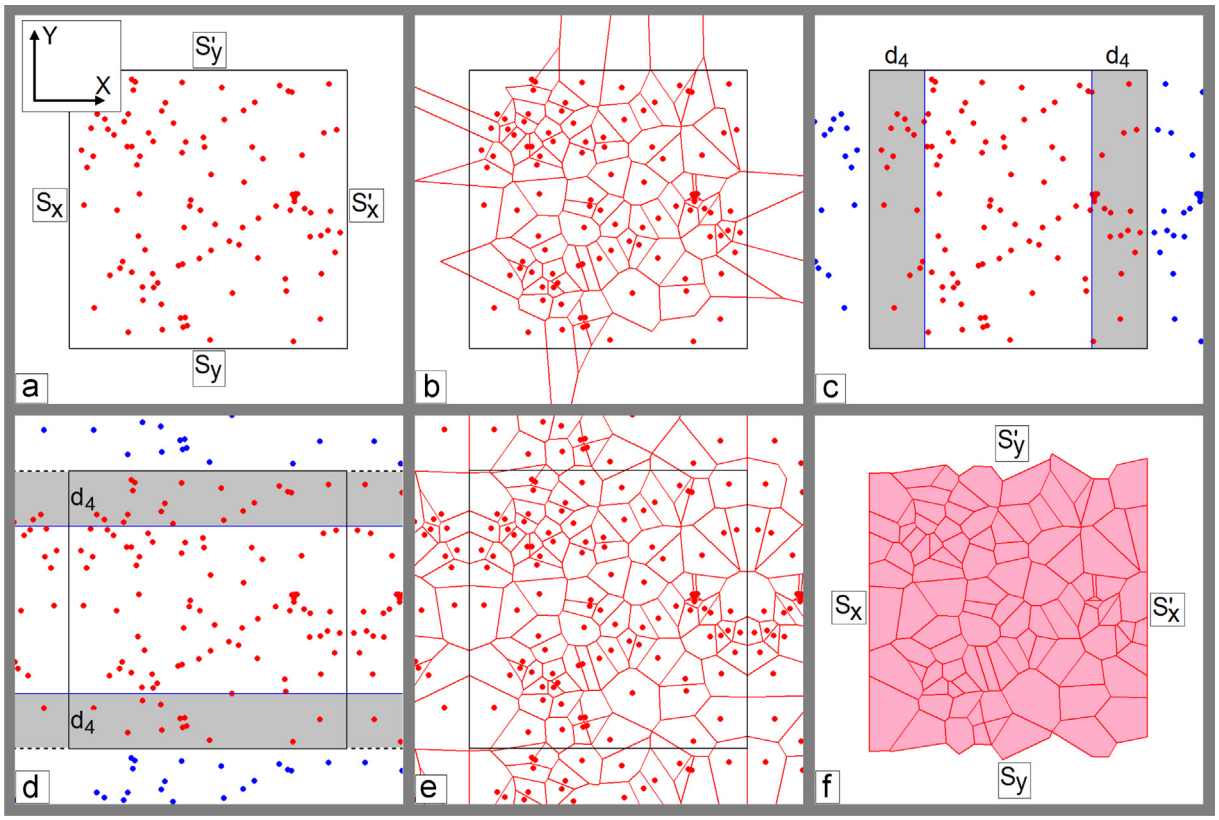

Fig. 5. 2D illustration of the technique used to apply wall-type geometric conditions along the *x*-direction and periodic geometric conditions along the *y*-direction.

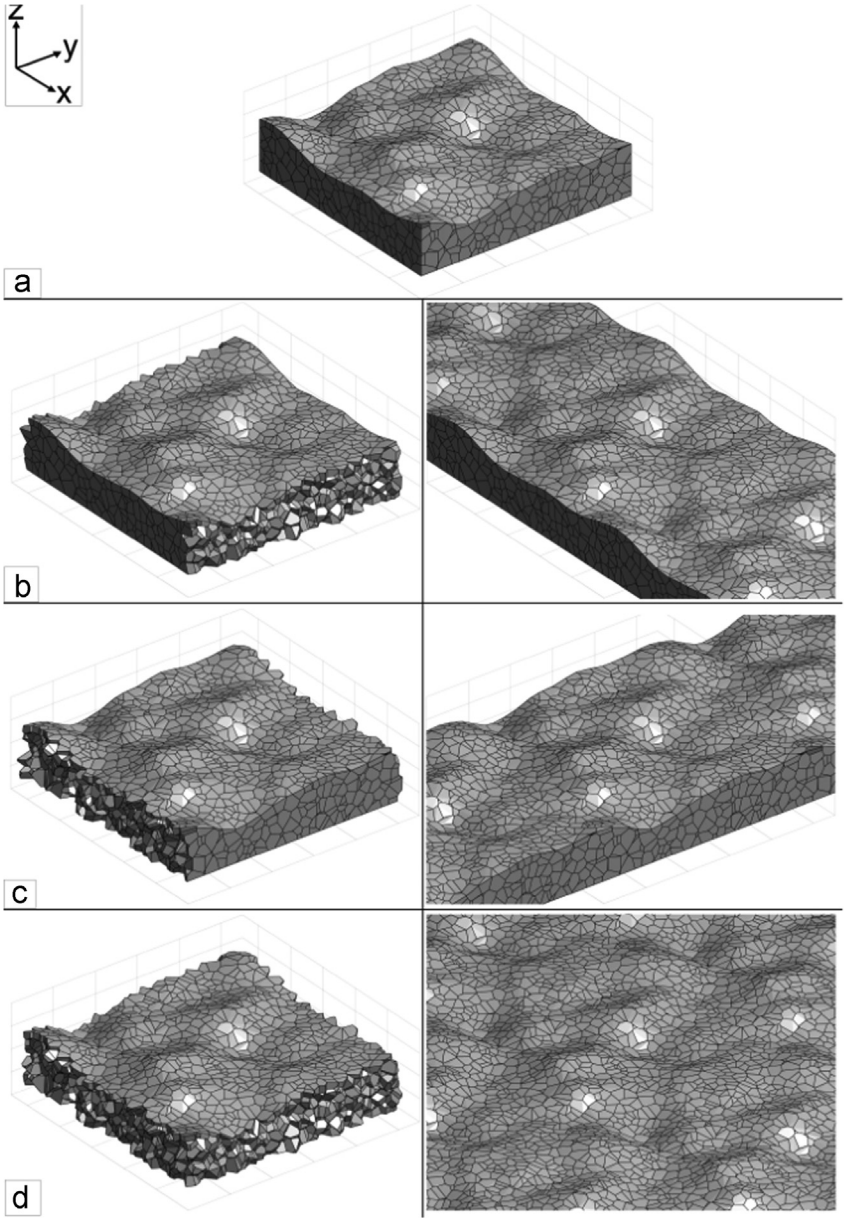

Fig. 6. Example of micro-structured degradable first-body containing 5000 grains, with a rough surface and various lateral conditions; (a) walls along x and y; (b) x-periodicity; (c) y-periodicity; (d) bi-periodicity.

Fig. 8d and e illustrates the cases of anisotropic microstructures which may occur in some particular materials. In Fig. 8d the grains are flat (their average vertical dimension is twice smaller than their average horizontal dimension), while in Fig. 8e they are vertically elongated (their average vertical dimension is twice larger than their average horizontal dimension). Such anisotropies cannot be easily introduced by simply acting on the initial set of seeding points, since any dilation of a random cloud of points will leave its isotropy unaltered. Alternatively, a simple technique is used here, based on a dilation of the microstructure itself. In the case of Fig. 8d, for example, the sample was generated using all the techniques presented earlier in this paper, but on a square domain of dimensions 0.5×0.5 instead of 1×1. Then, at the end of the generation, all the horizontal coordinates of the vertices of the cells were multiplied by a factor 2, resulting in this flat microstructure on the 1×1 domain. These operations did not disturb the frequency content of the upper surface, since all the modes introduced in the random surface generation are normalized with respect to the sample dimensions. On the contrary, in Fig. 8e, the sample was first generated on a 2×2 domain and its horizontal dimensions were then divided by 2.

In further developments, it seems possible to implement techniques allowing the introduction of inclined anisotropic microstructures, of controlled distributions of the grain size (like already proposed in [15,17,48]), or making it possible to have an even better control on all the features of the microstructure (see e.g. [49]).

3.3. Surface roughness

Fig. 9 illustrates the effect of the parameters introduced during the generation of the rough surfaces S_z and S_z' on the generated sample. Fig. 9a–c presents respectively a low-frequency roughness, a high-frequency roughness, and an anisotropic roughness of the upper surface S_z of the degradable first body. These different situations seem to be handled well by the generation algorithm, although Fig. 9b shows that it is difficult to render properly a desired very rough surface with a limited number of convex grains. Fig. 9d–f presents the same kind of results for the surface

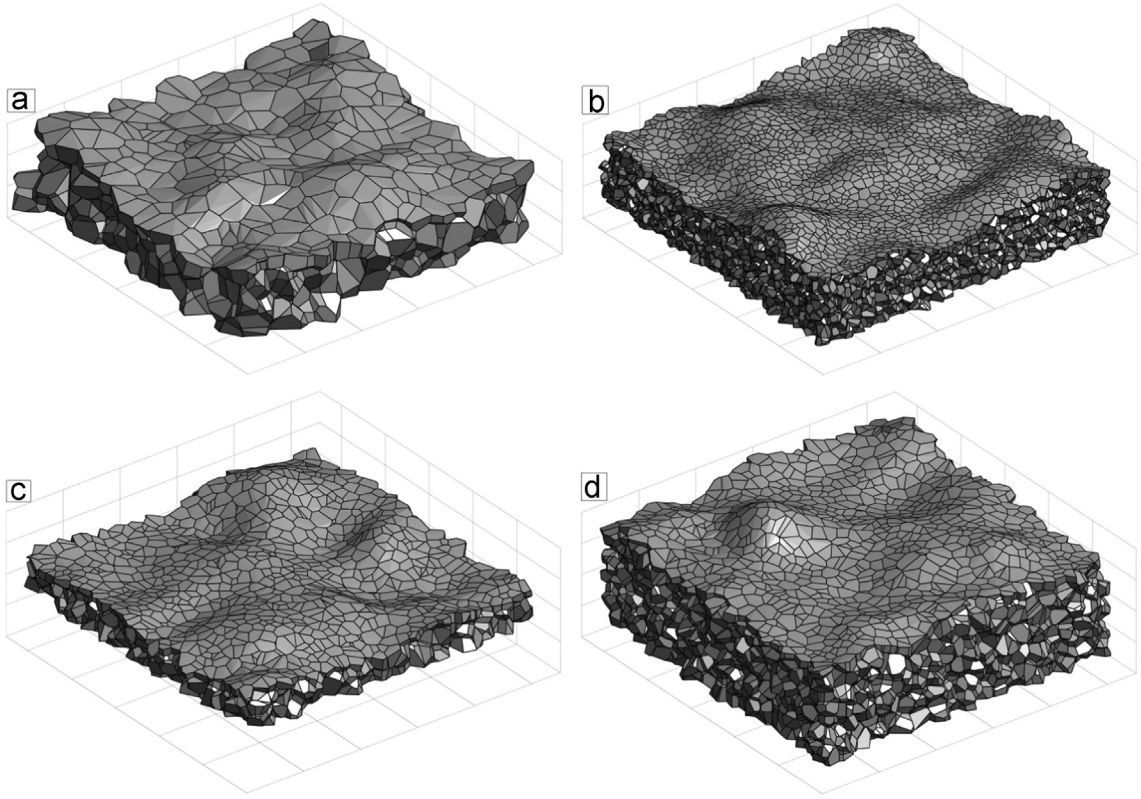

Fig. 7. Illustrative samples generated on the unit square domain with various average depths and numbers of cells.

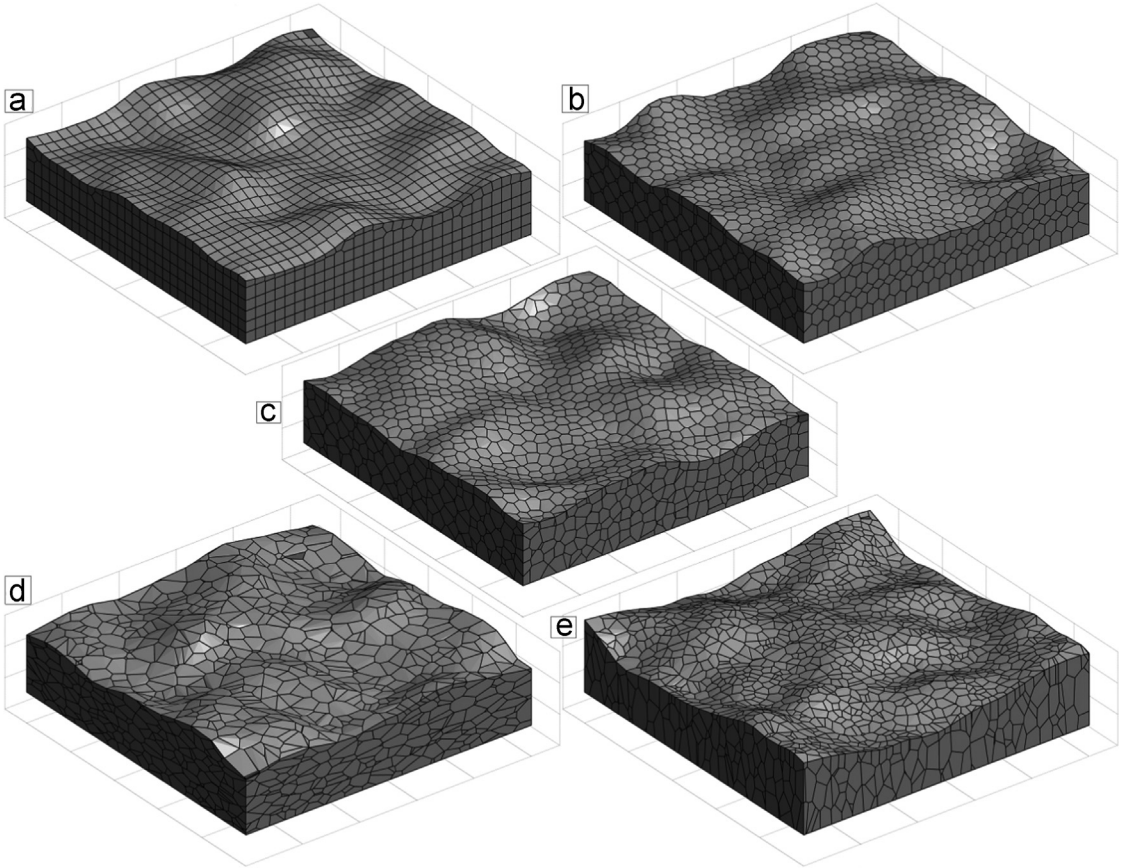

Fig. 8. Illustrative samples generated on the unit square domain with various inner microstructures.

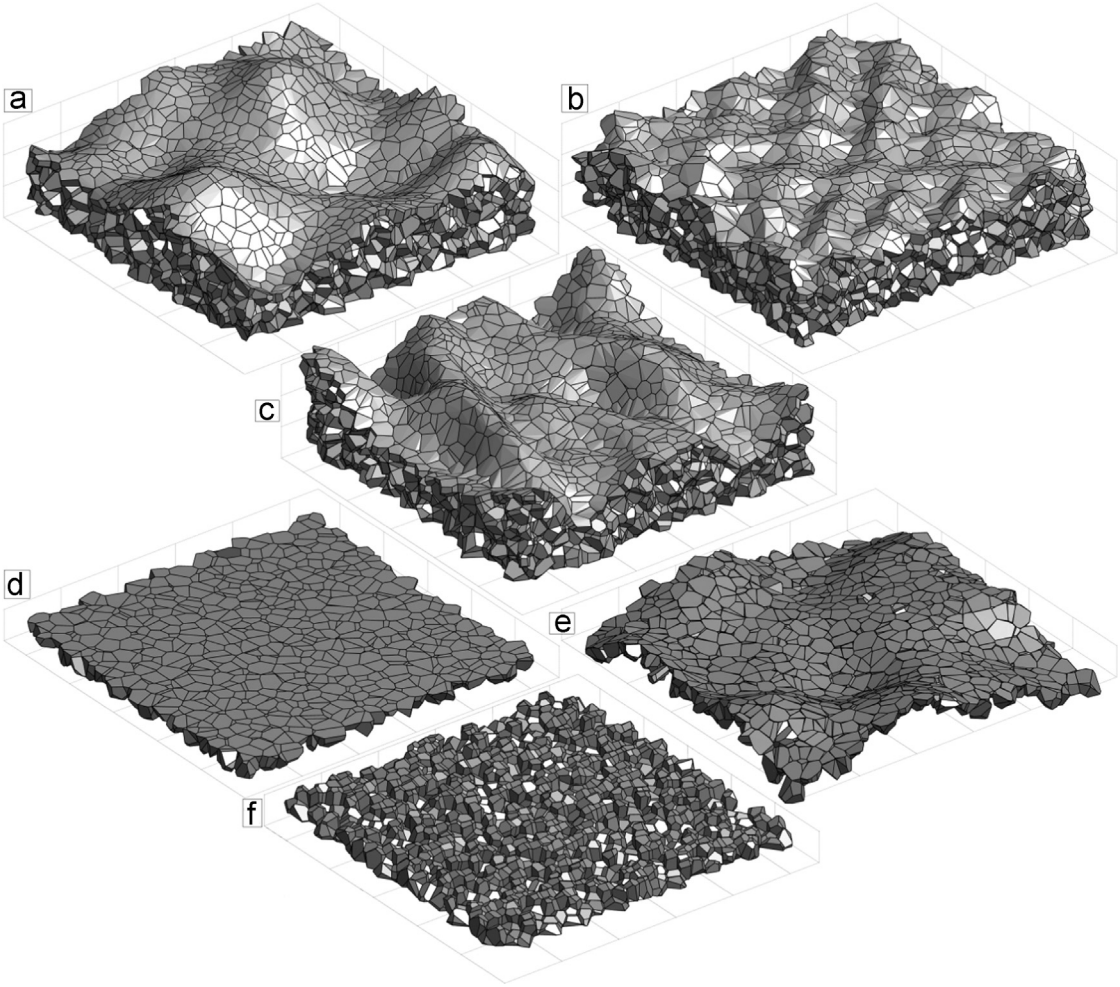

Fig. 9. Illustrative samples generated on the unit square domain with various types of surface roughness; (a)–(c) roughness of the upper surface S_z; (d)–(f) roughness of the lower surface S_z'

S_z' separating the degradable and the non-degradable parts of the first body. In Fig. 9d (flat interface) and e (low frequency roughness), the strategy described in Fig. 4g is applied, i.e. these interfaces respect the input statistics. In Fig. 9f, however, the strategy of Fig. 4h is applied, and an additional layer of cells is considered to belong to the non-degradable part of the first body. This way, the interface is globally flat but the microstructure is entangled in the same way than in the bulk of the material.

4. Illustrative simulation

4.1. Implementation in the NSCD framework

The Discrete Element Method is a well-known numerical modelling framework which was initially proposed by [7], and which is classically based on an explicit time-integration of the laws of motion of each grain composing a granular assembly. These laws of motion depend on the forces applied on each grain, and thus require the definition and calibration of proper contact laws which provide the possible attractive, repulsive, and frictional forces between the contacting grains. An alternative approach for dealing with multi-body multi-contact problems was later proposed in [50] and further developed in [51,52]: the Non-Smooth Contact Dynamics (NSCD) approach. In contrast with the classical DEM, the NSCD method is based on an implicit time-integration and a non-linear contact solver, and does not require such numerical regularization parameters as normal or tangential stiffness at contact (hence the "non-smooth" denomination). Among the advantages of the NSCD approach, one may mention the possibility to use larger time-steps than in the classical DEM, and the ability to couple in the same system of equations both rigid discrete elements and deformable continuous elements (using FEM). It has been widely used in many scientific and engineering fields. In the present work we make use of the open-source software LMGC90 [53], which implements all the features of the NSCD approach, together with a large choice of contact laws. Moreover, it is able to deal efficiently with complex particle shapes such as convex polyhedrons, by accounting for different types of contact such as node-face, edge-face, or edge-edge.

The samples generated using the method described in Section 2 may thus be introduced in this software, provided that a few "cleaning" operations are performed. The first operation consists in deleting a few particles that may be too small (e.g. with a volume smaller than 1% of the average grain volume) since they would complicate the dynamic simulation without having a significant mechanical contribution. For the same reason, we also ignore the particles which are too elongated (e.g. with a ratio between the largest and the smallest dimension larger than 20), although such particles usually do not occur if the geometrical boundaries are properly accounted for (Section 2). The last operation consists in "collapsing" the too short edges (e.g. shorter than 1% of the average edge length of the given cell) and the too small angles (e.g. smaller

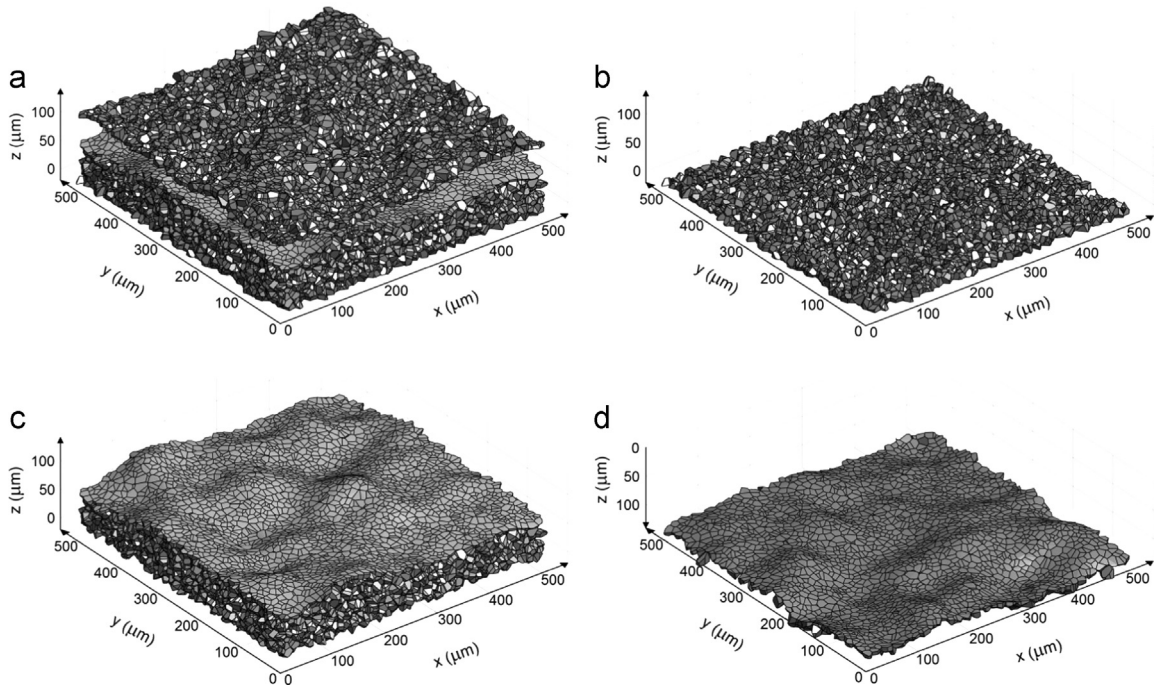

Fig. 10. Sample generated for discrete modelling; (a) full sample; (b) non-degradable part of the lower first-body (2498 grains); (c) degradable part of the lower first-body (21,925 grains); (d) upper non-degradable first-body (2583 grains, flipped upside-down to show topography).

than 1°) that often appear in the Voronoi cells. The algorithm developed for this purpose is very close to that proposed in [54] to overcome analogous difficulties.

4.2. Geometry, contact law and loading

The sample generated for simulation and introduced in LMGC90 is shown in Fig. 10a. It is composed of a lower first-body, with a degradable part and a non-degradable part, and of an upper first-body which is considered as non-degradable for the sake of simplicity. The horizontal dimensions are $500\ \mu m \times 500\ \mu m$, and the average depth of degradable material is $H = 80\ \mu m$. The sample contains about 27,000 polyhedral grains, with an average dimension of the grains close to $10\ \mu m$. The contacting surfaces of the upper first-body and of the degradable part of the lower first-body are randomly generated with the same parameters (i.e. $n_{x0} = n_{y0} = 2$, $\sigma = 8\ \mu m$, and $\lambda_x = \lambda_y = 0.5$, see Fig. 10c and d), and the interface between the degradable and the non-degradable parts of the lower first-body is globally flat but uses the approach of Fig. 4h to entangle properly the microstructure (Fig. 10b).

Since this sample is used here for illustrative purpose only, a very simple contact law is used for simulations. A non-interpenetration condition is implemented by the means of a Signorini condition, and a normal attractive cohesive force is introduced between contacting grains. This force is equal to $n \cdot c$, where n is the number of contact points used by LMGC90 to deal with complex contacts between polyhedrons (for example, $n \simeq 3$ or 4 for a face-face contact, $n = 1$ for an edge-edge contact, etc.) and c is set to 0.1 N in the present case. When applied to a real case, such simulation might require less crude contact laws, as discussed in the last section of this paper.

The sample is bi-periodic in the horizontal directions. The loading conditions applied to the sample are very classical, and similar to that usually applied when modelling this type of system. The six degrees of freedom of the non-degradable part of the lower first-body are fixed, while the upper first-body is considered as a unique rigid body, and is fixed in all its rotational degrees of freedom and in the y-direction translation. This rigid body is also submitted to an imposed velocity in the x-direction and to a downward force in the z-direction. This velocity and this force are applied following the timing detailed in Fig. 11: the vertical force is linearly increased from zero to a value F_z between $t = 0$ and $t = t_1$ and then fixed, while the imposed velocity is equal to zero until $t = t_1$, linearly increased to a value V_x until $t = t_2$, and then fixed. The chosen value for the vertical force is $F_z = -125$ N, corresponding to a moderate (500 MPa) local contact pressure. Besides, we set $V_x = 1\ m/s$, $t_1 = 10\ \mu s$, and $t_2 = 20\ \mu s$. The time step for the implicit integration of the laws of motion in the NSCD framework is set to 10^{-9} s, the total simulated time is $120\ \mu s$, and the simulation is launched on 16 CPU on the computation cluster of the LaMCoS.

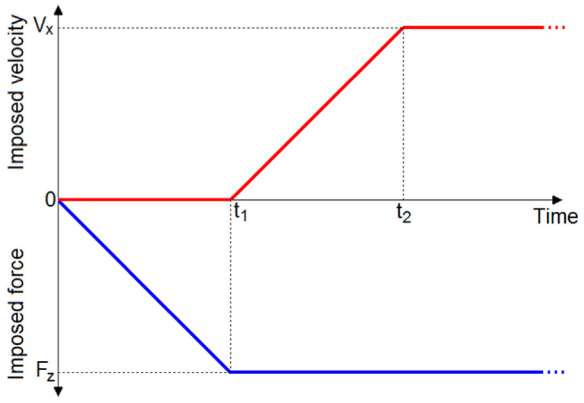

Fig. 11. Timing of the boundary conditions applied to the upper first-body.

4.3. Numerical results

Every $0.1\ \mu s$, the total normal and tangential forces applied on the moving upper first-body are computed, and an instantaneous mobilized friction is thus obtained. These "numerical measures" are plotted in Fig. 12, and appear to be strongly fluctuating. However, the application of a moving average to this discrete signal makes it possible to read the general trend of the system. Hence, we may observe that the mobilized friction increases

progressively until reaching a somewhat constant value (although very strongly fluctuating) at $t \approx 50$ μs. These fluctuations are to be related with local dynamic instabilities, force chains creations and breakages, etc. The average friction ratio corresponding to this established regime is close to 1, which is a very high value but may be realistic in some specific situations. In order to obtain a more realistic behaviour from a quantitative point of view, however, it is obvious that a proper calibration of the local contact laws seems necessary.

Fig. 13 provides a side-view and a perspective view of the sample at $t = 100$ μs, with the colours of the grains corresponding to their respective velocity magnitudes. It clearly appears that the grains belonging to the lower half of the degradable part of the lower first-body seem to remain still, and that the microstructure remains mostly unaltered in this region. On the contrary, the grains located in the upper half of the degradable body are submitted to motion, which means that the microstructure and the initial roughness of the surface have been completely degraded by the friction. This observation is in good agreement with the third-body theory, which states that the local friction is controlled by the rheology of the degraded material that friction itself has created. Fig. 13b also shows that the velocity field in the third-body layer is not homogeneous at all, and that some clusters of particles seem to be moving at a velocity close to that of the upper first-body while some others are moving more slowly. One may conclude that there is a high level of dynamic complexity in the third-body flow patterns, which might be interesting to study in order to understand their contribution on the macroscopic friction.

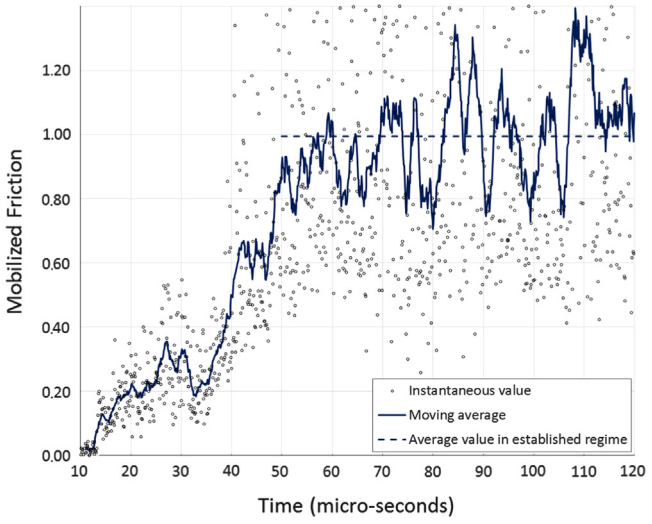

Fig. 12. Mobilized friction (i.e. ratio of the tangential and normal forces) along time during the simulation: Instantaneous values, moving average (with a 10 μs time span), and average value in established regime (after 50 μs).

Fig. 14 provides some quantitative support to the previous observations, by plotting the individual velocity of each grain as a function of its z-coordinate. The obtained velocity field is very heterogeneous and fluctuating, but the average velocity profile clearly shows that the microstructure of the lower first-body is mostly unaltered on the first 60 μm, and that the material is then submitted to a sheared flow on a depth of roughly 40 μm, which corresponds to the third-body layer. It also clearly appears that there is a velocity jump between the upper part of the third-body (with an average velocity $V_x = 0.4\ m/s$) and the upper first-body (with a fixed velocity $V_x = 1\ m/s$).

Obviously, the quantitative and qualitative results proposed in this section are not connected to the real behaviour of any system, since no calibration was performed on the contact laws, surface roughnesses, and material microstructures. It is clear that different modelling choices may lead to very different behaviours, which

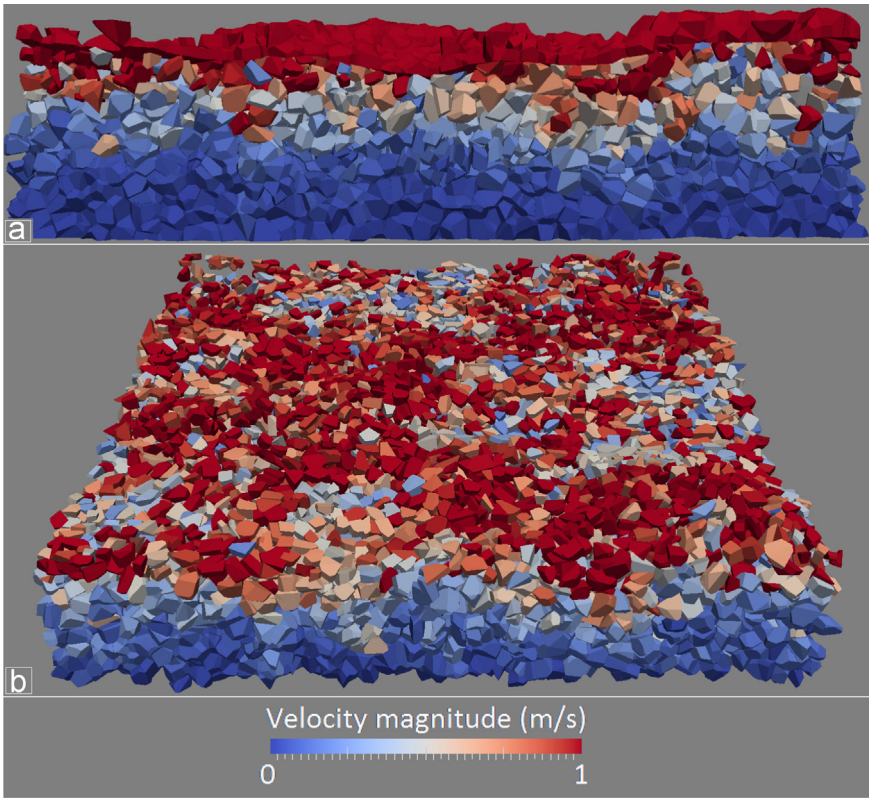

Fig. 13. Velocity magnitudes of the grains at $t = 100$ μs; (a) side view, including the upper substrate; (b) perspective view, with the upper substrate omitted for the sake of visibility.

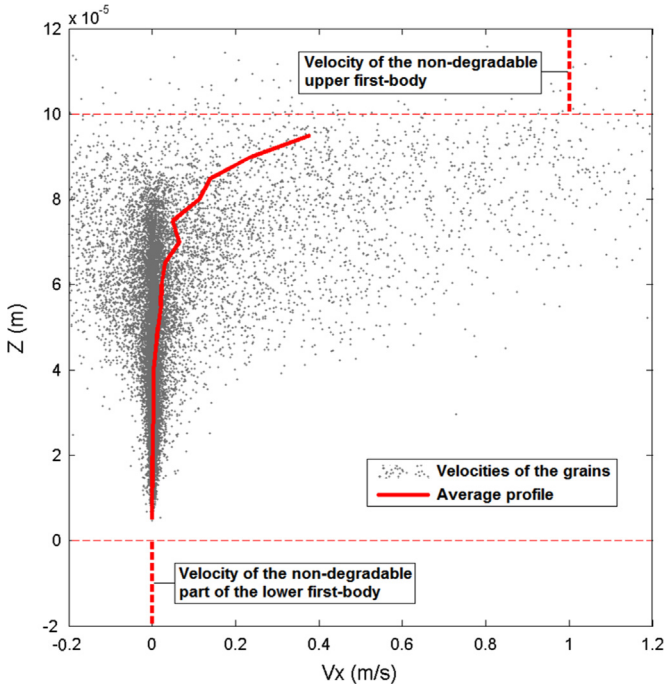

Fig. 14. Velocity magnitude of the grains at $t=100\,\mu s$ as a function of their z-coordinate, and corresponding average velocity profile.

may help to understand the connexions between the local scale and the global scale. This will be the topic of future studies.

5. Perspectives

Thanks to its generality and its flexibility, the numerical framework presented in this paper may have an interesting potential in future modelling of friction and wear in dry contacts. One important condition for this type of model to be realistic, however, is the implementation and use of more physical contact laws. For the grains belonging to the degradable first-body, such ingredients as normal and tangential contact stiffness (in order to represent more accurately the stress state in the bulk of the material and the Poisson effect, like for example in [38]) and a damage law (in order to represent the strength evolution at the grain joints submitted to complex loadings [26]) should be introduced in the model. On the other hand, for the grains belonging to the third-body (i.e. completely separated from the first-bodies), surface energy evolving with the physical environment of the grain (e.g. temperature, chemical reactivity [55] or gas contamination [56]) represents a promising trend.

From a purely mechanical point of view, a possible evolution of the model may account for the deformability of the non-degradable parts of the first bodies (in order to investigate the possible stress redistributions induced by the degradation of the first-bodies) or of the individual grains (in order to approach more realistically the phenomenology of the third-body, which might not always be considered as a granular collection of rigid bodies). Such approach may be implemented in LMGC90 thanks to the natural ability of NSCD to couple DEM and FEM. These possible evolutions, however, will require a proper calibration based on experimental observations and measurements.

Acknowledgement

The members of the team developing the LMGC90 software in the University of Montpellier, France (F. Dubois, R. Mozul, and M. Renouf) have been very helpful during this project, and are gratefully acknowledged.

References

[1] Godet M. The third-body approach: a mechanical view of wear. Wear 1984;100:437–52.
[2] Berthier Y. Experimental evidence for friction and wear modelling. Wear 1990;139:77–92.
[3] Descartes S, Berthier Y. Rheology and flows of solid third bodies: back-ground and application to an mos1.6 coating. Wear 2002;252(7–8):546–56.
[4] Berthier Y, Descartes S, Busquet M, Niccolini E, Desrayaud C, Baillet L, et al. The role and effects of the third body in the wheel–rail interaction. Fatigue Fract Eng Mater Struct 2004;27:423–36.
[5] Higgs III CF, Tichy JA. Granular flow lubrication: continuum modeling of shear behaviour. ASME J Tribol 2004;126:499–509.
[6] Higgs III CF, Tichy JA. Effect of particle and surface properties on granular lubrication flow. I Mech E 2008;222:703–13.
[7] Cundall PA, Strack ODL. A discrete numerical model for granular assemblies. Géotechnique 1979;29(1):47–65.
[8] Tillemans H-J, Herrmann H-J. Simulating deformations of granular solids under shear. Phys Rev A 1995;217:261–88.
[9] Mollon G, Zhao J. Characterization of fluctuations in granular hopper flows. Granular Matter 2013;15(6):827–40.
[10] Pournin L, Weber M, Tsukahara M, Ferrez J-A, Ramaioli M, Liebling TM. Three-dimensional distinct element simulation of spherocylinder crystallization. Granular Matter 2005;7(2):119–26.
[11] Azema E, Radjai F, Saussine G. Quasistatic rheology, force transmission and fabric properties of a packing of irregular polyhedral particles. Mech Mater 2009;41:729–41.
[12] Ferellec J-F, McDowell G. A method to model realistic particle shape and inertia in DEM. Granular Matter 2010;12:459–67.
[13] Richefeu V, Mollon G, Daudon D, Villard P. Dissipative contacts and realistic block shapes for modelling rock avalanches. Eng Geol 2012;19(150):78–92.
[14] Mollon G, Richefeu V, Villard P, Daudon D. Numerical simulation of rock avalanches: influence of a local dissipative contact model on the collective behavior of granular flows. J Geophys Res Solid Earth 2013;117:F02036.
[15] Mollon G, Zhao J. Fourier–Voronoi-based generation of realistic samples for discrete modelling of granular materials. Granular Matter 2012;14:621–38.
[16] Mollon G, Zhao J. Generating realistic 3D sand particles using Fourier descriptors. Granular Matter 2013;15(1):95–108.
[17] Mollon G, Zhao J. "3D generation of realistic granular samples based on random fields theory and Fourier shape descriptors". Comput Methods Appl Mech Eng 2014;279:46–65.
[18] Katagiri J, Matsushima T, Yamada Y. Simple shear simulation of 3D irregularly-shaped particles by image-based DEM. Granular Matter 2010;12:491–7.
[19] Matsushima T, Katagiri J, Uesugi K, Tsuchiyama A, Nakano T. 3D shape characterization and image-based DEM simulation of the Lunar soil simulant FJS-1. J Aerosp Eng 2009;22(1):15–23.
[20] Hall SA, Bornert M, Desrues J, Pannier Y, Lenoir N, Viggiani G, et al. Discrete and continuum analysis of localised deformation in sand using X-ray μCT and volumetric digital image correlation. Géotechnique 2010;60(5):315–22.
[21] Elrod HG, Brewe DE. Numerical experiments with flows of elongated granules. Tribol Ser 1991;21:219–26.
[22] Lubrecht AA, Berthier Y. Granular lubrication; a simple model and trends. Tribol Ser 1995;30:53–62.
[23] Ghaouti A, Chaze M, Dubujet P, Sidoroff F. Particulate and granular simulation of the third body behaviour. Tribol Ser 1996;31:355–65.
[24] Johnson KL, Kendall K, Roberts AD. Surface energy and the contact of elastic solids. Proc R Soc London A 1971;324:301–13.
[25] Seve B, Iordanoff I, Berthier Y. A discrete solid third body model: influence of the intergranular forces on the macroscopic behaviour. Tribol Interface Eng Ser 2001;39:361–8.
[26] Champagne M, Renouf M, Berthier Y. Modeling wear for heterogeneous bi-phasic materials using discrete elements approach. ASME J Tribol 2014;136 (2):021603.
[27] Fillot N, Iordanoff I, Berthier Y. A granular dynamic model for the degradation of material. ASME J Tribol 2004;126(3):606–14.
[28] Fillot N, Iordanoff I, Berthier Y. Simulation of wear through a mass balance in a dry contact. ASME J Tribol 2005;127(1):230–7.
[29] Renouf M, Saulot A, Berthier Y. Third body flow during a wheel–rail interaction. In: Mota Soares CA, editor. III European conference on computational mechanics solids; 2006.
[30] Saulot A, Renouf M, Berthier Y. Fem-dem dialogue for tribological understanding. In: Proceedings of the ASME/STLE international joint tribology conference; 2008.
[31] Fillot Renouf M. Coupling electrical and mechanical effects in discrete element simulations. Int J Numer Methods Eng 2008;74:238–54.
[32] Richard D, Iordanoff I, Renouf M, Berthier Y. Thermal study of the dry sliding contact with third-body presence. ASME J Tribol 2008;130(3):031404.
[33] Blok HA. Theoretical study of temperature rise at surface at actual contact under oilness lubricating conditions. I Mech E 1937;2:222–35.

[34] Potapov AV, Campbell CS, Hopkins MA. A two-dimensional dynamic simulation of solid fracture part I: description of the model. Int J Mod Phys C 1995;6(3):371–98.
[35] Potapov AV, Campbell CS, Hopkins MA. A two-dimensional dynamic simulation of solid fracture part II: examples. Int J Mod Phys C 1995;6(3):399–425.
[36] Thornton C, Kafui DK. Computer simulated impact of agglomerates. Powders Grains 1993;93:401.
[37] Meguro K, Hakuno M. Fracture analyses of concrete structures by the modified distinct element method. Proc Jpn Soc Civ Eng 1989;410:113–24.
[38] Raje N, Sadeghi F, Rateick RG. A discrete element approach to evaluate stresses due to line loading on an elastic half-space. Comput Mech 2007;40:513–29.
[39] Raje N, Sadeghi F, Rateick RG, Hoeprich MR. Evaluation of stresses around inclusions in Hertzian contacts using the discrete element method. J Tribol 2007;129:283–91.
[40] Raje N, Slack T, Sadeghi F. A discrete damage mechanics model for high cycle fatigue in polycristalline materials subject to rolling contact. Int J Fatigue 2009;31:346–60.
[41] Al-Samarai RA, Haftirman Ahmad KR, Al-Douri Y. Evaluate the effects of various surface roughness on the tribological characteristics under dry and lubricated conditions for Al – Si alloys. J Surf Eng Mater Adv Technol 2012;2:167–73.
[42] Parthasarathi NL, Borah U, Albert SK. Correlation between coefficient of friction and surface roughness in dry sliding wear of AISI316L(N) Stainless steel at elevated temperatures. Comput Model New Technol 2013;17(1):51–63.
[43] Soulie M, Montes P, et Silvestri V. Modelling spatial variability of soil parameters. Can Geotech J 1990;27:617–30.
[44] Fenton GA, Griffiths DV. Bearing capacity prediction of spatially random $C-\varphi$ soils. Can Geotech J 2003;40:54–65.
[45] Mollon G, Phoon K-K, Dias D, Soubra A-H. Validation of a new 2D failure mechanism for the stability analysis of a pressurized tunnel face in a spatially varying sand. J Eng Mech, ASCE 2011;137(1):1–14.
[46] Shinozuka M, et Deodatis G. Simulation of stochastic processes by spectral representation. Appl Mech Rev, ASME 1991;44(4):191–204.
[47] Phoon KK, Huang HW, Quek ST. "Simulation of strongly non-Gaussian processes using Karhunen – Loeve expansion.". Prob Eng Mech 2005;20(2):188–98.
[48] Xu T, Li M. Topological and statistical properties of a constrained Voronoi tessellation. Philos Mag 2009;89-4:349–74.
[49] Sonon B, François B, Massart TJ. A unified Level set based methodology for fast generation of complex microstructural multi-phase RVEs. Comput Methods Appl Mech Eng 2012;223–224:103–22.
[50] Moreau J-J. Une formulation du contact `a frottement sec; application au calcul numérique. Comptes Rendus Acad Sci Paris, Ser II 1986;302:779–801.
[51] Moreau JJ. Some numerical methods in multibody dynamics: application to granular materials. EurJ Mech A 1994;13(4):93–114.
[52] Jean M. The non-smooth contact dynamics method. Comput Methods Appl Mech Eng 1999;177(3 – 4):235–57.
[53] Dubois F, Jean M. LMGC90 une plateforme de développement dédiée à la modélisation des problèmes d'interaction. Giens, France: *Actes du sixième colloque national en calcul des structures*; 2003.
[54] Weinzapfel N, Sadeghi F, Bakolas V. An approach for modeling material grain structure in investigations of Hertzian subsurface stresses and rolling contact fatigue. J Tribol 2010;132:011404.
[55] Riviere J, Renouf M, Berthier Y. Simulation du comportement thermique d'un milieu continu équivalent par la méthode des éléments discrets. 11 – 17 of May. 11è Colloque National en Calcul des Structures 2013:2013 in French.
[56] Colas G, Saulot A, Godeau C, Michel Y, Berthier Y. Describing third body flows to solve dry lubrication issue – MoS2 case study under ultrahigh vacuum. Wear 2013;305(1 – 2):192–204.